

Drug delivery micelles with efficient near-infrared photosensitizer for combined image-guided photodynamic therapy and chemotherapy of drug-resistant cancer



Shijie Zhen^{a,1}, Xiaoqing Yi^{b,d,1}, Zujin Zhao^{a,*}, Xiaoding Lou^{b,**}, Fan Xia^b, Ben Zhong Tang^{a,c,***}

^a State Key Laboratory of Luminescent Materials and Devices, Center for Aggregation-Induced Emission, South China University of Technology, Guangzhou, 510640, China

^b Engineering Research Center of Nano-Geomaterials of Ministry of Education, Faculty of Materials Science and Chemistry, China University of Geosciences, 388 Lumo Road, Wuhan, 430074, China

^c Department of Chemistry, Hong Kong Branch of Chinese National Engineering Research Center for Tissue Restoration and Reconstruction, The Hong Kong University of Science and Technology, Clear Water Bay, Kowloon, Hong Kong, China

^d College of Pharmacy, Gannan Medical University, Ganzhou, 341000, China

ARTICLE INFO

Keywords:

Near-infrared fluorophore
Photosensitizer
Photodynamic therapy
Chemotherapy
Drug delivery

ABSTRACT

The combination of photodynamic therapy (PDT) and chemotherapy (CT) offers a promising approach for the tumor eradication for overcoming multidrug resistance (MDR), which is a major obstacle to effective cancer treatment. However, for PDT, simultaneously achieving near-infrared (NIR) emission and efficient reactive oxygen species (ROS) generation with low dark toxicity is urgently needed but remains challenging. Herein, a series of novel fluorophores with strong NIR emission, hybridized local and charge transfer characteristics, good two-photon absorption, high photostability, low dark cytotoxicity and excellent ROS generation ability are developed. By encapsulating the NIR fluorophore (DEB-BDFO) as a photosensitizer along with a drug resistance inhibitor tariquidar (TQR) within a polymeric prodrug (PMP), a reduction-sensitive drug co-delivery system (DEB/TQR@PMP micelles) is constructed. The DEB/TQR@PMP micelles exhibit a prominent synergistic lethal effect of PDT and CT on SKOV-3 cells and SKOV-3/MDR cells, and can apparently enhance the inhibition of tumor growth compared with sole PDT or CT in the tumor-bearing mouse model. Both in vitro and in vivo experiments prove that the new NIR fluorophores are excellent photosensitizers and can furnish an efficient combination therapy of image-guided PDT and CT within drug delivery micelles, which is particularly useful for eradicating multidrug resistance cancer.

1. Introduction

Nowadays, cancer is a serious disease for human being, causing an estimated 9.6 million cancer deaths in 2018 [1]. Chemotherapy (CT) is one of the most widely used cancer treatment but its efficacy is often greatly weakened due to the emergence of multidrug resistance (MDR), a common phenomenon that cancer cells become resistant to the cytotoxicity of chemotherapeutic agents and eventually leads to the death of patients from distant metastases [2,3]. In addition to the major obstacle of MDR, the conventional sole-model CT also suffers from systemic toxicity by non-specific drug distribution, poor bioavailability

and impaired target specificity, causing severe nausea and vomiting, hair loss, and frequent tiredness and weakness [2,4]. One of the promising approaches to address these issues is the combination therapy because of the low recurrence risk and high efficiency [5,6]. Early combination therapy is formulated by simply mixing two or more drugs, but their performances are largely limited by the inability to control the amount and appropriate ratio of each drug at the target tissue [7]. Current researches reveal that combining CT with image-guided photodynamic therapy (PDT) can provide a feasible and effective strategy for resolving these problems owing to the synergistic, complementary tumor eradication effect elicited by the two therapy

* Corresponding author.

** Corresponding author.

*** Corresponding author. State Key Laboratory of Luminescent Materials and Devices, Center for Aggregation-Induced Emission, South China University of Technology, Guangzhou, 510640, China.

E-mail addresses: mszjzhao@scut.edu.cn (Z. Zhao), louxiaoding@cug.edu.cn (X. Lou), tangbenz@ust.hk (B.Z. Tang).

¹ These authors contribute equally.

approaches [8,9]. In addition, drug delivery systems are often employed to maximize therapy efficacy and diminish the differences in pharmacokinetic profiles [5,10]. Among numerous drug delivery systems, those based on biocompatible and biodegradable amphiphilic polymeric micelles have received increasing scientific interest and have been widely adopted owing to its capability to achieve selective tumor targeting by enhanced permeability and retention (EPR) effect [11–14].

PDT is an emerging noninvasive treatment modality which relies on photosensitizer and light to generate reactive oxygen species (ROS) to kill cancer cells, and has gained considerable attention owing to its controllable property and high spatiotemporal resolution, thus offering a promising alternative for cancer treatment [15–19]. Ideal reagents for image-guided PDT should possess several desirable features, such as strong photosensitization for target ablation under light irradiation, NIR emission for deep-tissue imaging, good photostability, and negligible dark toxicity [19,20]. Recently, some photosensitizers with NIR emission based on porphyrin [21,22], BODIPY [23,24] and cyanine [25,26] have been reported for image-guided PDT. However, the porphyrin derivatives usually have rigid, planar and hydrophobic structures, and are prone to form tight aggregate in aqueous media, which induces strong intermolecular interactions and thus dramatically reduces their fluorescence and ROS production [22]. For BODIPY derivatives, they often encounter obvious dark toxicity and low fluorescence caused by heavy atoms [23]. And for cyanine derivatives, the moderate ROS generation ability limit their practical application in PDT [26]. Therefore, the design of efficient NIR photosensitizers that can fully meet the requirements for high-performance image-guided PDT is still technically challenging.

In this work, we wish to report a series of novel NIR fluorophores with excellent ROS generation ability (DMA-BDTO, DEA-BDTO and MPPZ-BDTO) based on a 4,8-bis((2-ethylhexyl)oxy)benzo[1,2-*b*:4,5-*b'*]dithiophene 1,1,5,5-tetraoxide (BDTO) core (Fig. 1A). The encapsulation of DEA-BDTO and a drug resistance inhibitor tariquidar (TQR) using polymeric prodrug poly(ethylene glycol)-*b*-poly(5-methyl-5-propargyl-1,3-dioxan-2-one)-*g*-paclitaxel, PEG-*b*-PMPMC-*g*-PTX (PMP), yields a reduction-sensitive drug co-delivery system, in which NIR fluorophore DEA-BDTO functions as a photosensitizer for image-guided PDT, and PMP that contains a paclitaxel (PTX) polymeric prodrug serves CT. The combination therapy of image-guided PDT and CT provides superior therapeutic effect against MDR cancer.

2. Results and discussion

The new NIR fluorophores with a BDTO core are facilely prepared according to the synthetic routes illustrated in Fig. 1A. 4,8-Bis((2-ethylhexyl)oxy)benzo[1,2-*b*:4,5-*b'*]dithiophene (DBr-BDT) underwent oxidation with 3-chloroperoxybenzoic acid (*m*CPBA) to provide intermediate 2,6-dibromo-4,8-bis((2-ethylhexyl)oxy)benzo[1,2-*b*:4,5-*b'*]dithiophene 1,1,5,5-tetraoxide (DBr-BDTO) [27], followed by the couplings with corresponding arylboronic acids to yield DMA-BDTO, DEA-BDTO and MPPZ-BDTO. The detailed synthetic procedures and characterization data are described in Supporting Information (Figs. S1–S9). They have good thermal stability, as evidenced by high decomposition temperatures (T_d) of 292–315 °C (Fig. S10 and Table 1). DEA-BDTO crystallizes into triclinic crystal system in hexane and dichloromethane mixture. The single crystal structure of DEA-BDTO indicates that it adopts a relatively planar conformation of the conjugated molecular backbone with a small torsion angle of 16.38° between BDTO and *N,N*-diethylaniline (Fig. 1B), which is conducive to electronic coupling between the fragments. The interplanar distances between neighbouring DEA-BDTO molecules in crystals are 3.402–3.495 Å (Fig. S11), indicating the existence of the π - π stacking interactions between DEA-BDTO molecules.

The absorption maxima of these new fluorophores are located in the range of 514–546 nm in tetrahydrofuran (THF) (Fig. 1C), which are associated with the formation of charge transfer state from peripheral

electron-donating nitrogen-containing groups to electron-withdrawing BDTO core [27]. The fluorophores show large absorptivity of $3.25 \times 10^4 \text{ L M}^{-1} \text{ cm}^{-1}$ at 532 nm for DMA-BDTO, $5.05 \times 10^4 \text{ L M}^{-1} \text{ cm}^{-1}$ at 546 nm for DEA-BDTO and $4.91 \times 10^4 \text{ L M}^{-1} \text{ cm}^{-1}$ at 514 nm for MPPZ-BDTO. The molecularly dispersed fluorophores exhibit photoluminescence (PL) peaks at ~642 nm (Fig. 1C) in THF solutions, with high fluorescence quantum yields (Φ_F s) of 46.1–63.2% (Table 1). They possess large Stokes shifts. For instance, the Stokes shift of MPPZ-BDTO is 127 nm, which is highly preferred to reduce light scattering and self-absorption. In addition, the dipole moments of DEA-BDTO are further estimated from the PL spectra in different solvents (Fig. 1D) on the basis of the Lippert-Mataga relation. The dipole moment of 15.33 D in high-polar solvents ($f > 0.15$) indicates the existence of the charge transfer state, while 9.50 D in low-polar solvents ($f < 0.15$) is resulted from the locally excited state (Fig. 1E) [27]. The hybridized local and charge transfer (HLCT) state can be formed due to the interaction between charge transfer state and locally excited state [28,29]. In solid state, DMA-BDTO, DEA-BDTO and MPPZ-BDTO exhibit NIR emission peaking at 739, 723 and 670 nm (Fig. 1F), respectively, with high Φ_F s of 10.1–12.9%. The solid-state Φ_F of 12.9% at 739 nm is much higher than those of many reported organic NIR fluorophores in the literature [30–32]. Two-photon absorption (TPA) spectra of the fluorophores are investigated in the range of 800–1200 nm (Fig. 1G). The maximum TPA cross section values of DMA-BDTO, DEA-BDTO and MPPZ-BDTO are 330, 368 and 419 GM ($1 \text{ GM} = 1 \times 10^{-50} \text{ cm}^4 \text{ s photon}^{-1} \text{ molecule}^{-1}$) on excitation at 820 nm, respectively, measured using Rhodamine 6G in methanol as reference [33]. The ROS generation ability of DMA-BDTO, DEA-BDTO and MPPZ-BDTO is further investigated using 2',7'-dichlorofluorescein diacetate (DCFH-DA) as probe under white light irradiation (40 mW cm^{-2}). As shown in Fig. 1H, the three NIR fluorophores, particularly DEA-BDTO, exhibit much better ROS generation efficiencies than DCFH-DA, but slightly poorer than chlorine e6 (Ce6). The new NIR fluorophores with large two-photon absorption cross sections and high ROS generation efficiency could be very promising materials for two-photon excited photodynamic therapy.

The optimized geometrical and electronic structures of these NIR fluorophores are theoretically calculated by density functional theory (DFT) at the basis set level of 6-31G(d,p). The torsion angles between BDTO and *N,N*-diethylaniline, *N,N*-diethylaniline and 1-methyl-4-phenylpiperazine are 22.6°, 21.8° and 19.1° (Fig. S12), respectively, indicating good planarity of the molecular backbones, which is consistent with the crystal structure. The highest occupied molecular orbitals (HOMOs) are mainly centered on the whole molecular backbones, while the lowest occupied molecular orbitals (LUMOs) are predominantly concentrated on the electron-withdrawing BDTO core (Fig. S13), indicating the fluorophores are prone to form charge transfer state, which is in good agreement with their photophysical properties (Fig. 1D). The practical energy levels of these fluorophores are also evaluated by cyclic voltammetry (Fig. S14). DMA-BDTO and DEA-BDTO reveal similar reversible oxidation and reduction process, while MPPZ-BDTO only shows oxidation process, indicating better electrochemical redox activity of DMA-BDTO and DEA-BDTO. The HOMO and LUMO energy levels of DMA-BDTO, DEA-BDTO and MPPZ-BDTO are estimated to be in the range of $-5.19 \sim -5.22 \text{ eV}$, and $-3.13 \sim -3.18 \text{ eV}$, respectively (Table 1).

Recently, drug delivery nanosystems, such as polymeric micelles, polymeric vesicles, nanogels, inorganic nanoparticles and liposomes, have shown high importance in anticancer treatment [34,35], owing to their excellent drug loading content via the EPR effect. In view of the excellent Φ_F in NIR region and efficient ROS generation efficiency of DEA-BDTO (abbreviated as DEB), we construct a reduction-sensitive co-delivery system of DEB/TQR@PMP micelles by encapsulating the NIR emissive photosensitizer DEB as well as a drug resistance inhibitor TQR within the micelles of polymeric prodrug PMP (Fig. 2) that is synthesized according to our previous reports [36,37]. The critical micelle

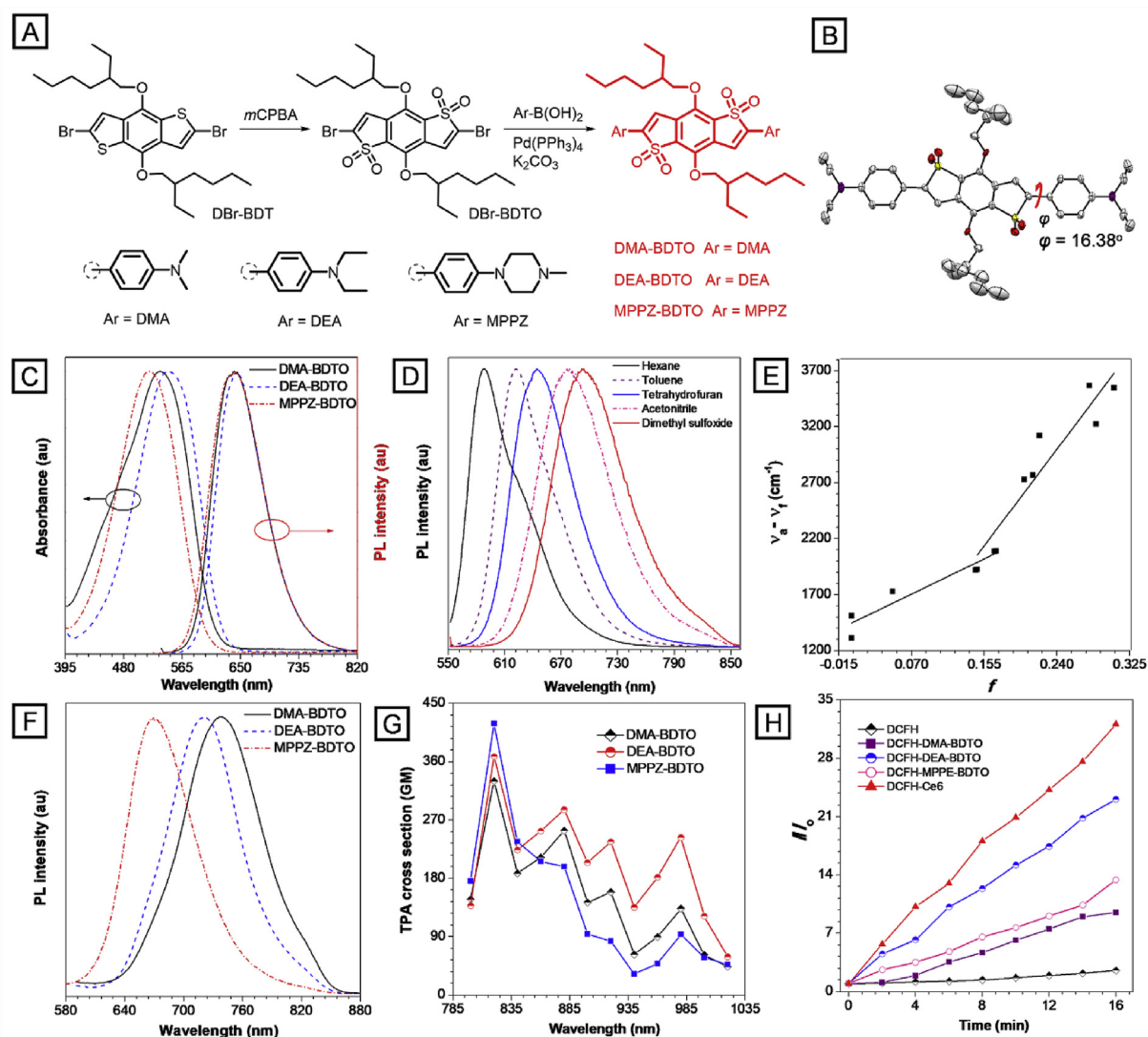


Fig. 1. (A) Synthetic routes toward NIR fluorophores based on BDTO. (B) ORTEP drawing of the crystal structure of DEA-BDTO. (C) Normalized absorption and PL spectra of NIR fluorophores in THF (10^{-5} M). (D) Normalized PL spectra of NIR fluorophores in different solvents. (E) Linear correlation of orientation polarization (f) of solvent media with the Stokes shifts ($\nu_a - \nu_f$) for DEA-BDTO. (F) Normalized PL spectra of NIR fluorophores in solid. (G) Two-photon absorption spectra of NIR fluorophores in THF (10^{-5} M). (H) Plots of I (emission intensity)/ I_0 (emission intensity at 0 min) of DCFH, DCFH/DMA-BDTO, DCFH/DEA-BDTO, DCFH/MPPZ-BDTO and DCFH-Ce6 versus different light irradiation time.

concentration (CMC) of PMP is 8.6 mg/L in aqueous solution (Table S1), determined by fluorescence measurement using pyrene as a probe. The DEB/TQR@PMP micelles are prepared by self-assembly of amphiphilic polymeric prodrug PMP, DEB and TQR (Fig. 2A). For comparison, PMP, DEB@PMP and TQR@PMP are also prepared and investigated.

Dynamic light scattering (DLS) measurement shows that the hydrodynamic sizes of PMP, TQR/PMP, DEB/PMP and DEB/TQR@PMP micelles are 118.1 nm (PDI = 0.294), 161.1 nm (PDI = 0.257), 106.1 nm (PDI = 0.225) and 157.0 nm (PDI = 0.244), respectively (Figs. 3A and S15, Table S1). As shown in Fig. S16 A and B, the TEM images confirm

Table 1
Optical properties and energy levels of the fluorophores based on BDTO.

	$\lambda_{\text{abs}}^{\text{a)}$ (nm)		$\lambda_{\text{em}}^{\text{b)}$ (nm)		$\Phi_{\text{F}}^{\text{b)}$ (%)		$\tau^{\text{c)}$ (ns)		HOMO/LUMO ^{d)} (eV)	$E_{\text{g}}^{\text{e)}$ (eV)	T_{d} (°C)
	THF ^{a)}	solid	THF ^{a)}	solid	THF ^{a)}	solid	THF ^{a)}	solid			
DMA-BDTO	532	642	739	62.1	12.9	2.36	2.58	−5.20/−3.16	2.04	292	
DEA-BDTO	546	641	723	63.2	10.1	3.23	3.64	−5.19/−3.18	2.01	308	
MPPZ-BDT	514	641	670	46.1	10.2	2.21	2.65	−5.22/−3.13	2.09	315	

^a In THF solution (10^{-5} M).

^b Fluorescence quantum yield, determined by a calibrated integrating sphere.

^c Fluorescence lifetime, measured at room temperature in air.

^d Determined by cyclic voltammetry in dichloromethane.

^e Optical bandgap calculated from the onset of absorption spectrum.

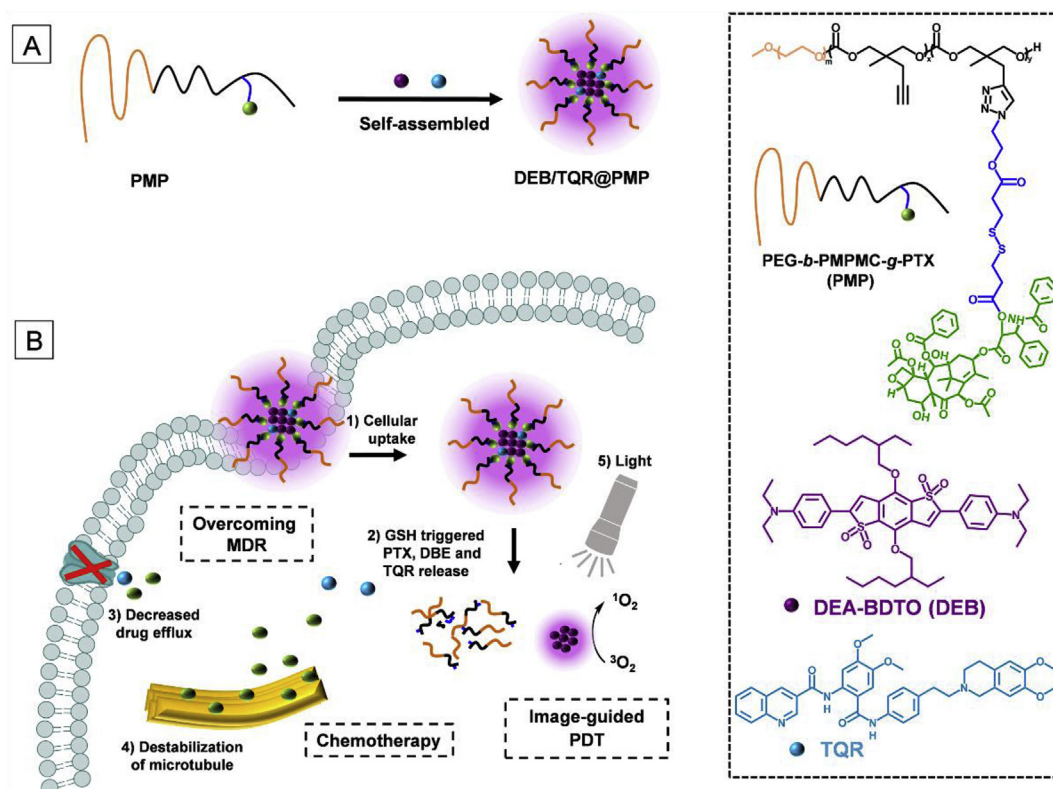


Fig. 2. (A) Schematic illustration of the preparation of DEB/TQR@PMP micelles and (B) its internalization and therapy process. Reduction-sensitive co-delivery system DEB/TQR@PMP can target tumor interstitial fluid in a passive manner via the EPR effect. After cleavage of disulfide bonds under high concentration of glutathione (GSH) in tumor cells, free PTX is released to disrupt the microtubule. Meanwhile, DEB generates cytotoxic ROS to damage the tumor cell under light irradiation. The co-delivery of TQR, a P-glycoprotein drug efflux pump inhibitor, results in significant inhibition of drug resistance.

that DEB@PMP and DEB/TQR@PMP micelles have a sharply defined sphere shape, with smaller size than corresponding DLS results, due to the shrinkage of PEG shells during the drying process [38,39]. The DEB/TQR@PMP micelles show absorption maximum at around 539 nm, a strong PL peak at around 690 nm and a relatively high Φ_F of 7.1% (Fig. 3B). A large Stokes shift of 151 nm is observed for DEB/TQR@PMP micelles, which is beneficial to in vivo bioimaging with high contrast and low background. In addition, the DEB/TQR@PMP micelles exhibit excellent stability after storage for 30 days in aqueous solution at room temperature (Fig. 3C).

It is well known that the disulfide bonds can be cleaved under intracellular reductive conditions, while they are stable in human blood plasma. Dithiothreitol (DTT), which can mimic intracellular reductive conditions, is used to investigate the release of PTX, TQR and DEB from DEB/TQR@PMP micelles in aqueous solution. PTX, TQR and DEB are released with higher rates in the presence of 10 mM DTT than that without DTT (Figs. 3D, E and 3F). Moreover, TQR is released faster than PTX in the condition of 10 mM DTT. For example, the release percentage of PTX (Fig. 3D, about 9%) is much smaller than that of TQR (Fig. 3E, about 33%) within 2 h. Also, 10 mM GSH is used as the reducing agent to study the release behaviors of PTX and TQR from DEB/TQR@PMP micelles in vitro (Fig. 3G and H). The release behaviors of PTX and TQR have little difference between 10 mM GSH and 10 mM DTT conditions. PTX is released in a sustained manner in response to reductive environment and accumulated in cells, achieving the intracellular drug release and finally reversing MDR [40]. TQR is released to inhibit the activity of P-glycoprotein (P-gp), especially in drug resistant cells, as confirmed in Fig. 3I. The expression level of P-gp in drug resistant SKOV-3/MDR cells is higher than those in drug-sensitive HeLa and SKOV-3 cells.

Meanwhile, the time-dependent size changes of PMP, DEB@PMP and DEB/TQR@PMP micelles under 10 mM DTT are investigated by

DLS. As shown in Fig. S15, the sizes of the three micelles are obviously increased in the presence of 10 mM DTT, due to the cleavage of the disulfide bonds by DTT, resulting in the detachment of PTX from the micelles and thus allowing PTX and TQR to aggregate through hydrophobic interactions [37]. In addition, the increased size is also due to the increased hydrophilic property of the residual polymer by leaving PTX and forming hydroxyl groups [41,42]. Meanwhile, the morphology of DEB/TQR@PMP micelles after incubation with 10 mM DTT is disintegrated rapidly. As shown in Fig. S16C, upon exposure to 10 mM DTT, the size of spherical nanoparticles is increased, with an average diameter of 70–90 nm, and other worm-like morphology can also be observed. To keep track of the micelles, the effect of reduction-sensitive property of DEB@PMP and DEB/TQR@PMP micelles on the fluorescence intensity of DEB is investigated. As shown in Fig. S17, in the presence of 10 mM DTT, no obvious changes are observed for fluorescence intensity, indicating the fluorescence of DEB@PMP and DEB/TQR@PMP micelles displays high resistance to the reducing environments. The ROS generation ability of DEB/TQR@PMP micelles is evaluated by using 9,10-anthracenediyl-bis-(methylene) dimaleonic acid (ABDA) as a probe. With time elapsing, the peak at 400 nm decreases after 20 min of light irradiation (Fig. S18), demonstrating that DEB/TQR@PMP micelles can produce ROS efficiently. In addition, the ROS generation ability of DEB@PMP is better than that of DEB, as proved by Fig. S19.

The prodrug DEB/TQR@PMP micelles can be quickly cleaved after endocytosis by tumor cells to rapidly release the active drug and consequently achieve cancer cell cytotoxicity resulting from EPR effect. The disassociated TQR can bind with P-gp to retrain its activity and reduce the efflux of anticancer drug PTX, and further to reverse MDR of tumor cells (Fig. 2B). Meanwhile, the disassociated DEB can efficiently generate ROS for PDT in cancer treatment. The intracellular ROS generation abilities of DEB@PMP and DEB/TQR@PMP micelles in HeLa

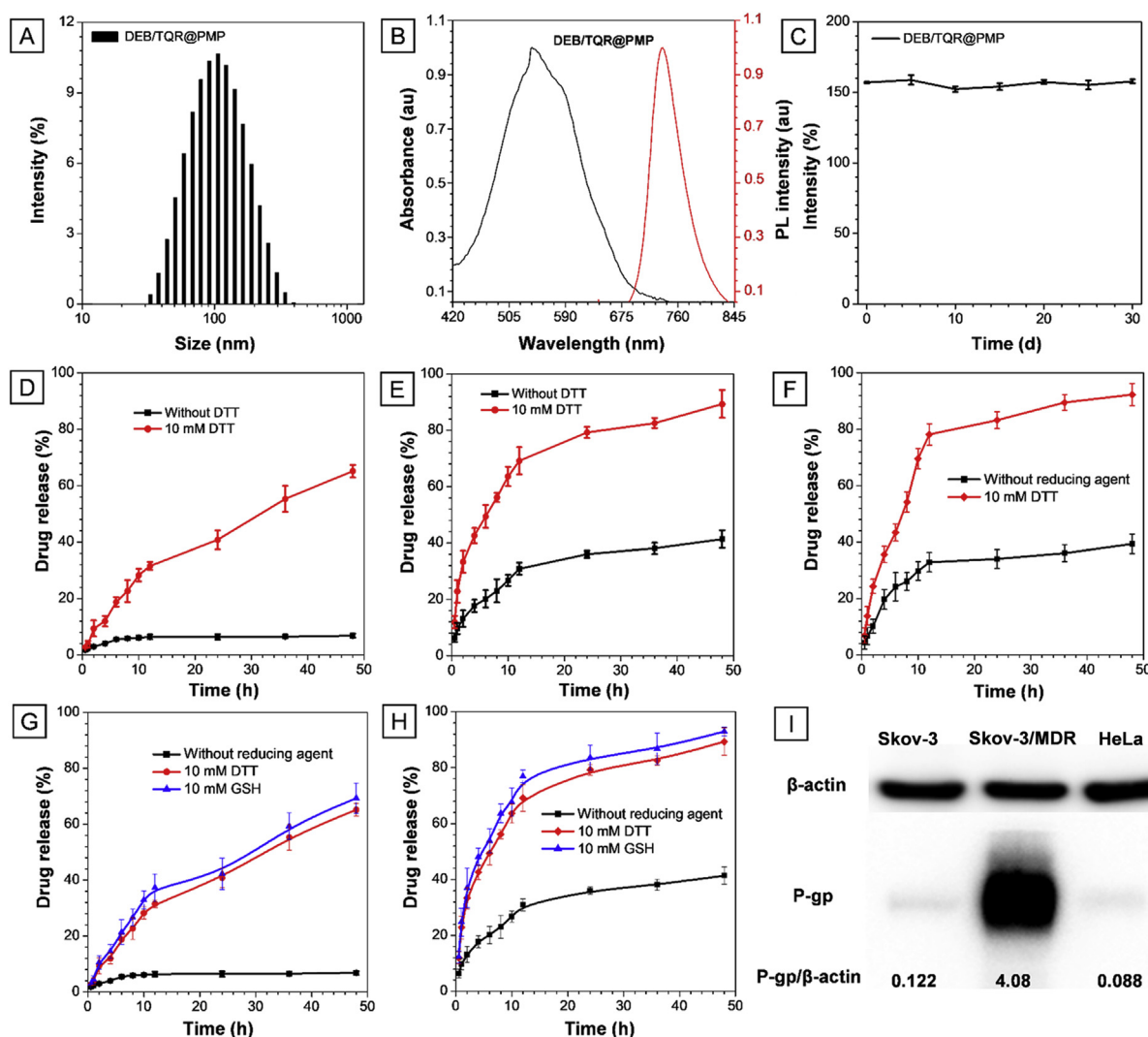


Fig. 3. (A) Hydrodynamic size distribution of DEB/TQR@PMP micelles. (B) Normalized absorption and PL spectra of DEB/TQR@PMP micelles in aqueous solution. (C) Stability of DEB/TQR@PMP micelles in PBS during 30-day storage at room temperature. In vitro release of PTX (D), TQR (E) and DEB (F) from DEB/TQR@PMP micelles in PBS (pH 7.4, 0.1 M) containing 0.1% (w/v) tween 80 at 37 °C with 10 mM DTT or without DTT, respectively. In vitro release of PTX (G) and TQR (H) from DEB/TQR@PMP micelles in PBS (pH 7.4, 0.1 M) containing 0.1% (w/v) tween 80 at 37 °C without reducing agent, with 10 mM DTT and with 10 mM GSH, respectively. (I) Expressions of P-gp in SKOV-3 cells, SKOV-3/MDR cells and HeLa cells.

cells, SKOV-3 cells and SKOV-3/MDR cells are assessed using as ROS sensor, as shown in Figs. 4A and S20. After incubation with DEB@PMP or DEB/TQR@PMP micelles for 4 h without light irradiation, only weak green fluorescence is detected in HeLa cells, SKOV-3 cells and SKOV-3/MDR cells. Under light irradiation, remarkable green fluorescence is observed in HeLa cells, SKOV-3 cells and SKOV-3/MDR cells incubated with DEB@PMP or DEB/TQR@PMP micelles. This is due to that non-fluorescent DCFH-DA is oxidized to green fluorescent DCFH by ROS produced from DEB@PMP and DEB/TQR@PMP micelles. These results indicate that DEB-loaded micelles can be used for PDT.

To reduce the efflux of exotic hydrophobic drug and enhance the therapy efficacy. P-gp inhibitor TQR is co-loaded in DEB@PMP micelles during the preparation of the micelles. PTX-sensitive HeLa cells, PTX-sensitive SKOV-3 cells and SKOV-3/MDR cells are used as cell models to investigate the cellular imaging. As shown in Figs. 4B and S21, after incubation with DEB@PMP and DEB/TQR@PMP micelles, obvious fluorescence signals can be observed for HeLa cells, SKOV-3 cells and SKOV-3/MDR cells. However, for SKOV-3/MDR cells, DEB/TQR@PMP micelles exhibit apparently enhanced intracellular fluorescence intensity as compared with DEB@PMP. In other words, in the presence of TQR, the intracellular concentration of exotic hydrophobic drug is

increased in the drug resistant cells.

In order to investigate the effect of reducing PTX on the microtubule integrity, the micelles of PM, PMP, TQR@PM and TQR@PMP are incubated with HeLa cells, SKOV-3 cells and SKOV-3/MDR cells, respectively. Microtubules are accurately identified by confocal laser scanning microscopy (CLSM) using α -Tubulin-FITC antibody as an indicator. As shown in Figs. 4C and S22, there are no obvious morphological changes of microtubules observed for HeLa cells, SKOV-3 cells and SKOV-3/MDR cells after incubated with PM micelles and TQR@PM micelles, respectively. When treated with PMP micelles and TQR@PMP micelles, for PTX-sensitive HeLa cells, PTX-sensitive SKOV-3 cells, the microtubules are shrunk and damaged, which can be attributed to the cleavage of disulfide bonds and the release of PTX under intracellular reducing conditions. The released PTX can promote the assembly of tubulin in cancer cells and prevent its depolymerization, causing replication failure of aggregation and deaggregation, and then inducing cancer cells apoptosis. However, for PTX-insensitive SKOV-3/MDR cells, PMP micelles does not affect the morphological of microtubules. While incubated with TQR@PMP micelles, serious disruption and damage to the microtubules are observed (Fig. 4C). The results indicate that the co-delivery system based on polymeric prodrug micelles can

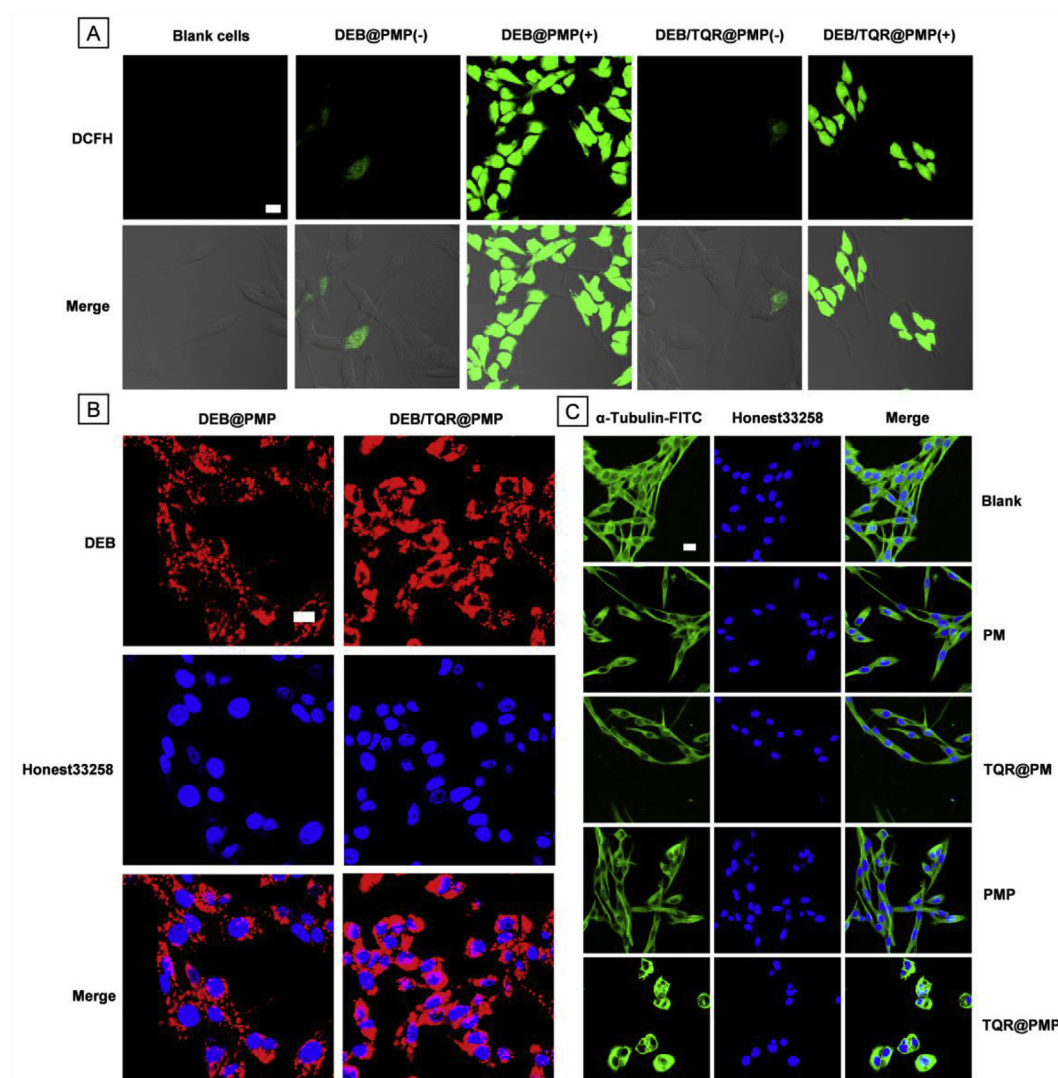


Fig. 4. (A) Detection of intracellular ROS production by DCFH-DA in SKOV-3/MDR cells after incubation with DEB@PMP (–), DEB@PMP (+), DEB/TQR@PMP (–) and DEB/TQR@PMP (+) micelles, with light irradiation (+) or without light irradiation (–) (white light, 100 mW/cm², 3 min). Scale bar = 20 μm. (B) Confocal fluorescence images of SKOV-3/MDR cells stained by DEB@PMP, DEB/TQR@PMP micelles. The nuclei are stained by Hoechst 33258. Scale bar = 20 μm. (C) Detection of microtubules by α-Tubulin-FITC in SKOV-3/MDR cells after incubated with PM, TQR/PM, PMP and TQR/PMP micelles, respectively. Scale bar = 20 μm.

greatly enhance drug delivery into SKOV-3/MDR cells and, at the same time, significantly improve the accumulation of PTX by inhibiting the expression of *P-gp* in SKOV-3/MDR cells.

To investigate the cell inhibitory effect and the reversal of drug resistance by different micelles, the cytotoxicity of micelles is evaluated by CCK-8 assay using SKOV-3 cells, drug resistant SKOV-3/MDR cells. With light irradiation, PM micelles and TQR against SKOV-3 and SKOV-3/MDR cells are first tested, and no apparent cytotoxicity is found (Fig. S23). As shown in Fig. 5A and B, these drug-loaded micelles except DEB/TQR@PMP (+) micelles exhibit lower cytotoxicity than free PTX with an increasing PTX concentration ranging from 0.23 to 30.0 μg/mL against SKOV-3 cells. The half-maximal inhibitory concentration (IC₅₀) values of free PTX (–), PMP (–), DEB@PMP (–), DEB@PMP (+), TQR@PMP (–) and DEB/TQR@PMP (+) micelles are measured to be ~0.53, ~5.92, ~6.17, ~3.13, ~3.53 and ~0.22 μg/mL, respectively. It is found that DEB/TQR@PMP (+) micelles give an enhanced cell-growth inhibition at a low concentration of PTX by the combination of PDT and CT. For SKOV-3/MDR cells, after being treated with a high concentration of free PTX (100 μg/mL), no apparent cytotoxicity is observed (Fig. 5A). It is reasonable because of the low intracellular accumulation of free PTX drug. The IC₅₀ values of PMP (–), DEB@PMP

(–), DEB@PMP (+), TQR@PMP (–) and DEB/TQR@PMP (+) micelles are ~25.06, ~25.35, ~12.13, ~7.19 and ~3.35 μg/mL, respectively. As compared with PMP (–), TQR@PMP (–) micelles exhibit a significantly improved inhibition efficacy, probably owing to the addition of *P-gp* inhibitor TQR that can enhance the cytotoxicity of PTX to SKOV-3/MDR via the inhibition of *P-gp*-mediated drug efflux. In addition, DEB@PMP (+) has an enhanced cell-growth inhibition compared to PMP (–) and DEB@PMP (–), demonstrating the improved therapeutic effect of combination therapy. Moreover, it is noteworthy that the antitumor activity of DEB/TQR@PMP (+) micelles is much higher than that of TQR@PMP (–) and DEB@PMP (+) micelles. Taken together, DEB/TQR@PMP (+) micelles have the best ability to inhibit the proliferation of SKOV-3/MDR cells, and hold great potential for multidrug delivery to overcome drug resistance in tumor treatments. In addition, the cell viability of DEB@PMP micelles toward L929 cells (normal cells) with or without irradiation is investigated. As shown in Fig. S24, the cytotoxicity of DEB@PMP (–) towards L929 cells is weak. The cell viability remains almost 80% even at a high PTX concentration of 7.50 μg/mL for DEB@PMP (–).

As we known, the hemolysis ratio of materials is supposed to be below 5% if they can be applied to intravenous injection [43]. As shown

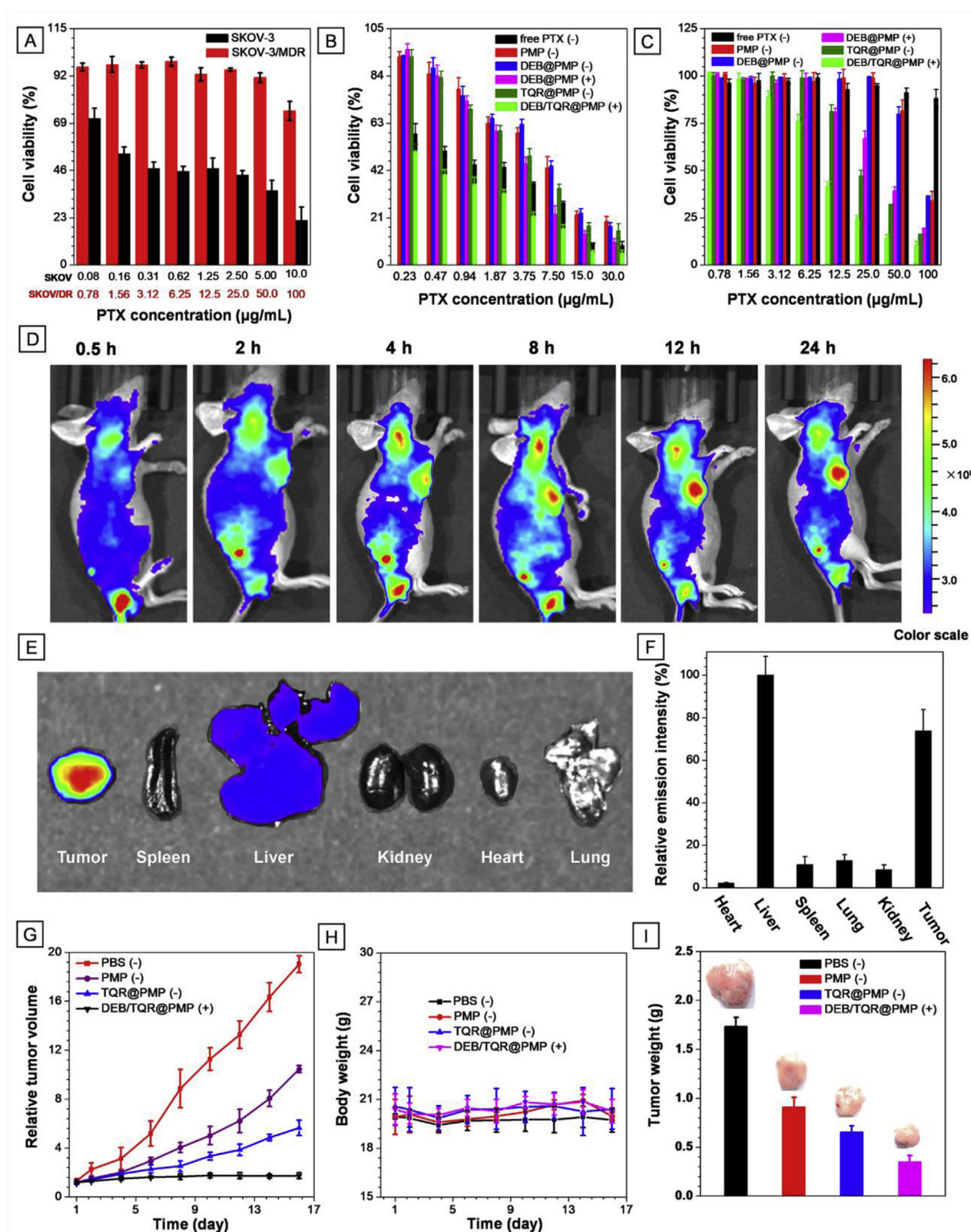


Fig. 5. (A) Viabilities of SKOV-3 cells and SKOV-3/MDR cells after incubation with different concentrations of PTX. CCK-8 assay of free PTX (-), PMP (-), DEB@PMP (-), DEB@PMP (+), TQR@PMP (-) and DEB/TQR@PMP (+) micelles in (B) SKOV-3 cells and (C) SKOV-3/MDR cells after incubation with different concentrations of PTX, with or without light irradiation. (D) Optical imaging of SKOV-3/MDR tumor-bearing mice after the intravenous injection of DEB/TQR@PMP micelles at different time. (E) Fluorescence images of the major organs and tumor and (F) relative emission intensity of the DEB/TQR@PMP micelles treated mice at 24 h post-injection. (G) Relative tumor volume, (H) tumor weight, and (I) body weight in the SKOV-3/MDR tumor-bearing mice after the intravenous of different samples: PBS (-), PMP (-), TQR@PMP (-) and DEB/TQR@PMP (+) micelles, with or without light irradiation.

in Fig. S25, the hemolysis ratios of PMP, DEB@PMP, TQR@PMP and DEB/TQR@PMP micelles are all below 4% even the concentration is as high as 200 $\mu\text{g/mL}$, indicating the micelles are suitable for intravenous injection. Further, the EPR effect-mediated accumulation process of DEB/TQR@PMP micelles in the tumor tissue is studied by using SKOV-3/MDR bearing mouse animal mode. The emission of DEB is utilized to trace the bio-distribution of DEB/TQR@PMP micelles. As shown in Fig. 5D, DEB/TQR@PMP micelles are gradually accumulated in tumor site and reach a maximum at about 12 h after administration. And negligible fluorescence signal is observed in heart, spleen, lung, and kidney, but strong fluorescence signals are found in tumor tissue and liver after injection of 24 h (Fig. 5E and F and S26). These results indicate that DEB/TQR@PMP micelles can selectively accumulate in tumor tissue.

The efficacy of DEB/TQR@PMP (+) micelles is evaluated by using SKOV-3 and SKOV-3/MDR bearing mouse animal mode, and PBS (–), PMP (–) and TQR@PMP (–) micelles are used as controls. Light irradiation is performed after 12 h injection in order that micelles can be absorbed effectively by tumor tissue without apparent drug metabolism. PMP (–) exhibits certain therapy efficacy to SKOV-3 and SKOV-3/MDR bearing tumor tissues (Figs. 5G, 5H, 5I and S26A, B, C). For TQR@PMP (–) micelles, they show enhanced therapy efficacy compared with PMP (–) to SKOV-3 and SKOV-3/MDR bearing tumor tissues, but still not good enough to effectively treat drug-resistant tumor models (Figs. 5G and S27A). It is gratifying that the DEB/TQR@PMP (+) can successfully reverse the multidrug resistance of tumors, and realize tumor inhibition by PTX, TQR and DEB loaded micelles upon light irradiation.

In addition, the mice body weight shows no obvious changes during the therapy in each group (Figs. 5H and S27C), while the tumor weights display notable differences between the mice treated with DEB/TQR@PMP micelles and other groups (Figs. 5I and S27B), indicating the enhanced therapeutic effect of combinational image-guided PDT and CT in vivo. Hematoxylin and eosin staining tumor tissues treated with PBS (–) are compact with few apoptotic or necrotic, while those incubated with PMP (–), TQR@PMP (–) and DEB/TQR@PMP (+) micelles are sparse, especially for tumor treated with DEB/TQR@PMP micelles, indicating they are more seriously apoptotic or necrotic in combinational therapy group (Figs. S28 and S27D). There is no obvious physiological morphology abnormality in heart, liver, spleen, lung, and kidney, confirming the low systemic toxicity for these samples.

3. Conclusions

In summary, a series of new efficient NIR fluorophores containing a BDTO core are synthesized and fully characterized by crystallography, spectroscopy, theory calculation, and electrochemistry. They exhibit strong NIR emission, good two-photon absorption property, high photostability, low dark cytotoxicity and excellent ROS generation ability. Particularly, DMA-BDTO acquires a high Φ_F of 12.9% at 739 nm in solid state, which is higher than most reported organic NIR fluorophores. A reduction-sensitive drug co-delivery system (DEB/TQR@PMP) comprised of a photosensitizer DEA-BDTO (DEB), a P-gp inhibitor TQR and a polymeric prodrug (PTX) is created for the combination therapy of image-guided PDT and CT. DEB/TQR@PMP micelles have strong NIR emission (690 nm), suitable particle size, excellent water stability and photostability, and can generate ROS efficiently in living cells. They exhibit synergistic enhancement effect of PDT and CT upon light irradiation to HeLa cells, SKOV-3 cells and SKOV-3/MDR cells. In the tumor-bearing mouse model, the DEB/TQR@PMP micelles can preferentially accumulate in the tumor tissue after intravenous injection and display enhanced inhibition of the tumor growth for overcome MDR by combining image-guided PDT and CT. In view of the good two-photon absorption ability, these new NIR fluorophores could have great potential to achieve image-guided combinational therapy with two-photon excitation technique.

4. Experimental

4.1. Synthesis

Synthesis of 2,6-bis(4-(dimethylamino)phenyl)-4,8-bis(heptan-3-yloxy)benzo[1,2-b:4,5-b']dithiophene 1,1,5,5-tetraoxide (DMA-BDTO): A mixture of 4-(dimethylamino)phenylboronic acid (660 mg, 4 mmol), DBr-BDTO (670 mg, 1 mmol), tetrakis(triphenylphosphine)palladium(0) (58 mg, 0.05 mmol) and potassium carbonate (553 mg, 4 mmol) was added into a 250 mL two-neck flask under nitrogen atmosphere. Then, a mixed solvent system of toluene, ethanol and water (v/v/v = 8:1:1) (120 mL) was injected into the bottle, and the mixture was refluxed over night. After cooling to room temperature, the mixture was poured into water and extracted three times with dichloromethane. The combined organic layers were washed successively with water, and then dried with anhydrous magnesium sulfate. After filtration, the solvent was evaporated under reduced pressure and the residue was purified by silica-gel column chromatography. Blackish green solid of DMA-BDTO was obtained in 60% yield. ^1H NMR (500 MHz, CDCl_3), δ (ppm): 7.71 (d, J = 8.95 Hz, 4H), 7.14 (s, 2H), 6.79 (d, J = 8.35 Hz, 4H), 4.38 (d, J = 5.55 Hz, 4H), 3.05 (s, 12H), 1.86–1.83 (m, 2H), 1.64–1.54 (m, 8H), 1.40–1.37 (m, 8H), 1.03 (t, J = 7.45 Hz, 6H), 0.95 (t, J = 6.95 Hz, 6H). ^{13}C NMR (125 MHz, CDCl_3) δ 151.43, 144.77, 142.67, 135.17, 131.39, 127.90, 127.39, 112.51, 112.25, 78.95, 40.44, 40.14, 30.29, 29.09, 23.73, 23.09, 14.13, 11.21. HRMS ($\text{C}_{40}\text{H}_{52}\text{N}_2\text{O}_6\text{S}_2$): m/z 748.3543 (M^+ , calcd 748.3580).

2,6-Bis(4-(diethylamino)phenyl)-4,8-bis(heptan-3-yloxy)benzo[1,2-b:4,5-b']dithiophene 1,1,5,5-tetraoxide (DEA-BDTO): The procedure was analogous to that described for DMA-BDTO. Blackish green solid of DEA-BDTO is obtained in 56% yield. ^1H NMR (500 MHz, CDCl_3), δ (ppm): 7.68 (d, J = 9.01 Hz, 4H), 7.08 (s, 2H), 6.71 (d, J = 8.10 Hz, 4H), 4.37 (d, J = 5.55 Hz, 4H), 3.41 (q, J = 7.05, 8H), 1.86–1.82 (m, 2H), 1.64–1.55 (m, 8H), 1.41–1.37 (m, 8H), 1.21–1.18 (m, 12H), 1.03 (t, J = 7.45 Hz, 6H), 0.95 (t, J = 6.90 Hz, 6H). ^{13}C NMR (125 MHz, CDCl_3) δ 149.13, 144.74, 142.72, 131.36, 128.16, 127.39, 113.44, 111.75, 111.68, 78.93, 44.54, 40.45, 30.30, 29.09, 23.74, 23.10, 14.13, 12.58, 11.22. HRMS ($\text{C}_{44}\text{H}_{60}\text{N}_2\text{O}_6\text{S}_2$): m/z 804.4188 (M^+ , calcd 804.4206).

4,8-Bis(heptan-3-yloxy)-2,6-bis(4-(4-methylpiperazin-1-yl)phenyl)benzo[1,2-b:4,5-b']dithiophene 1,1,5,5-tetraoxide (MPPZ-BDTO): The procedure is analogous to that described for DMA-BDTO. Green solid of MPPZ-BDTO is obtained in 55% yield. ^1H NMR (500 MHz, CDCl_3), δ (ppm): 7.71 (d, J = 9.01 Hz, 4H), 7.19 (s, 2H), 6.95 (d, J = 9.10 Hz, 4H), 4.38 (d, J = 5.50 Hz, 4H), 3.36 (t, J = 4.75 Hz, 8H), 2.57 (d, J = 4.05 Hz, 8H), 2.36 (s, 6H), 1.55–1.39 (m, 2H), 1.39–1.38 (m, 8H), 1.38–1.37 (m, 8H), 1.37–1.36 (m, 12H), 0.99 (t, J = 7.45 Hz, 6H), 0.94 (t, J = 6.95 Hz, 6H). ^{13}C NMR (125 MHz, CDCl_3) δ 152.29, 144.89, 142.43, 131.38, 127.91, 127.44, 116.87, 115.12, 114.04, 79.00, 54.70, 47.57, 46.10, 40.43, 30.30, 29.07, 23.73, 23.08, 14.13, 11.20. HRMS ($\text{C}_{46}\text{H}_{62}\text{N}_4\text{O}_6\text{S}_2$): m/z 858.4439 (M^+ , calcd 858.4424).

4.2. Crystal data for DEA-BDTO (CCDC 1828883)

$\text{C}_{46}\text{H}_{64}\text{N}_2\text{O}_6\text{S}_2$, M_w = 805.11, Triclinic, $P-1$, a = 9.4758(8) Å, b = 10.2553(11) Å, c = 11.5972(12) Å, α = 78.114(3)°, β = 87.040(3)°, γ = 78.433(3)°, V = 1080.36(19) Å³, Z = 1, D_c = 1.237 g cm^{−3}, μ = 0.0173 mm^{−1} (MoK α , λ = 0.71073), $F(000)$ = 434, T = 175(2) K, $2\theta_{\text{max}}$ = 25.242° (99.3%), 8862 measured reflections, 3915 independent reflections (R_{int} = 0.0859), GOF on F^2 = 1.044, R_1 = 0.1477, wR_2 = 0.1717 (all data), $\Delta\rho$ 0.475 and −0.312 eÅ^{−3}.

Acknowledgments

This work was financially supported by the National Natural Science Foundation of China (21788102, 21673082, 21525523 and 21722507),

the Guangdong Natural Science Funds for Distinguished Young Scholar (2014A030306035), the Natural Science Foundation of Guangdong Province (2019B030301003), and the China Postdoctoral Science Foundation (2018M643064). All the experimental procedures involved with animals were strictly performed under the guidelines of institution's IACUC (Institutional Animal Care and Use Committee).

Appendix B. Supplementary data

Supplementary data to this article can be found online at <https://doi.org/10.1016/j.biomaterials.2019.119330>.

Appendix A. Supplementary data

Supplementary data related to this article can be found in the online version.

References

- [1] F. Bray, J. Ferlay, I. Soerjomataram, R.L. Siegel, L.A. Torre, A. Jemal, Global cancer statistics 2018: GLOBOCAN estimates of incidence and mortality worldwide for 36 cancers in 185 countries, *Ca - Cancer J. Clin.* (68) (2018) 394–424.
- [2] C. Holohan, S. Van Schaeybroeck, D.B. Longley, P.G. Johnston, Cancer drug resistance: an evolving paradigm, *Nat. Rev. Cancer* (13) (2013) 714.
- [3] A. Persidis, Cancer multidrug resistance, *Nat. Biotechnol.* (17) (1999) 94.
- [4] M.L. Slevin, L. Stubbs, H.J. Plant, P. Wilson, W.M. Gregory, P.J. Armes, S.M. Downer, Attitudes to chemotherapy: comparing views of patients with cancer with those of doctors, nurses, and general public, *BMJ* (300) (1990) 1458–1460.
- [5] W. Fan, B. Yung, P. Huang, X. Chen, Nanotechnology for multimodal synergistic cancer therapy, *Chem. Rev.* (117) (2017) 13566–13638.
- [6] Y. Zhang, R. Sha, L. Zhang, W. Zhang, P. Jin, W. Xu, J. Ding, J. Lin, J. Qian, G. Yao, R. Zhang, F. Luo, J. Zeng, J. Cao, L.P. Wen, Harnessing copper-palladium alloy tetrapod nanoparticle-induced pro-survival autophagy for optimized photothermal therapy of drug-resistant cancer, *Nat. Commun.* (9) (2018) 4236.
- [7] R.K. Pathak, U. Basu, A. Ahmad, S. Sarkar, A. Kumar, B. Surnar, S. Ansari, K. Wilczek, M.E. Ivan, B. Marples, N. Kolishetti, S. Dhar, A designer bow-tie combination therapeutic platform: an approach to resistant cancer treatment by simultaneous delivery of cytotoxic and anti-inflammatory agents and radiation, *Biomaterials* (187) (2018) 117–129.
- [8] W. Chen, J. Ouyang, H. Liu, M. Chen, K. Zeng, J. Sheng, Z. Liu, Y. Han, L. Wang, J. Li, L. Deng, Y.-N. Liu, S. Guo, Black phosphorus nanosheet-based drug delivery system for synergistic photodynamic/photothermal/chemotherapy of cancer, *Adv. Mater.* (29) (2017) 1603864.
- [9] Y. Wang, M. Yang, J. Qian, W. Xu, J. Wang, G. Hou, L. Ji, A. Suo, Sequentially self-assembled polysaccharide-based nanocomplexes for combined chemotherapy and photodynamic therapy of breast cancer, *Carbohydr. Polym.* (203) (2019) 203–213.
- [10] M. Zhang, E. Liu, Y. Cui, Y. Huang, Nanotechnology-based combination therapy for overcoming multidrug-resistant cancer, *Cancer Bio. Med.* (14) (2017) 212–227.
- [11] W.-H. Chen, G.-F. Luo, W.-X. Qiu, Q. Lei, L.-H. Liu, D.-W. Zheng, S. Hong, S.-X. Zhang, X.-Z. Zhang, Tumor-triggered drug release with tumor-targeted accumulation and elevated drug retention to overcome multidrug resistance, *Chem. Mater.* (28) (2016) 6742–6752.
- [12] M.Q. Gong, J.L. Wu, B. Chen, R.X. Zhuo, S.X. Cheng, Self-assembled polymer/inorganic hybrid nanovesicles for multiple drug delivery to overcome drug resistance in cancer chemotherapy, *Langmuir* (31) (2015) 5115–5122.
- [13] Z. Dong, L. Feng, Y. Hao, M. Chen, M. Gao, Y. Chao, H. Zhao, W. Zhu, J. Liu, C. Liang, Q. Zhang, Z. Liu, Synthesis of hollow biomimetic hollow biomimeticized CaCO₃-polydopamine nanoparticles for multimodal imaging-guided cancer photodynamic therapy with reduced skin photosensitivity, *J. Am. Chem. Soc.* (140) (2018) 2165–2178.
- [14] Z. Meng, Y. Chao, X. Zhou, C. Liang, J. Liu, R. Zhang, L. Cheng, K. Yang, W. Pan, M. Zhu, Z. Liu, Near-infrared-triggered in situ gelation system for repeatedly enhanced photothermal brachytherapy with a single dose, *ACS Nano* (12) (2018) 9412–9422.
- [15] J.P. Celli, B.Q. Spring, I. Rizvi, C.L. Evans, K.S. Samkoe, S. Verma, B.W. Pogue, T. Hasan, Imaging and photodynamic therapy: mechanisms, monitoring, and optimization, *Chem. Rev.* (110) (2010) 2795–2838.
- [16] S.S. Lucky, K.C. Soo, Y. Zhang, Nanoparticles in photodynamic therapy, *Chem. Rev.* (115) (2015) 1990–2042.
- [17] X. Cai, D. Mao, C. Wang, D. Kong, X. Cheng, B. Liu, Multifunctional liposome: a bright AIEgen-lipid conjugate with strong photosensitization, *Angew. Chem. Int. Ed.* (57) (2018) 16396–16400.
- [18] C.Y.Y. Yu, H. Xu, S. Ji, R.T.K. Kwok, J.W.Y. Lam, X. Li, S. Krishnan, D. Ding, B.Z. Tang, Mitochondrion-anchoring photosensitizer with aggregation-induced emission characteristics synergistically boosts the radiosensitivity of cancer cells to ionizing radiation, *Adv. Mater.* (29) (2017) 1606167.
- [19] F. Hu, S. Xu, B. Liu, A highly efficient and photostable photosensitizer with near-infrared photosensitizers with aggregation-induced emission: materials and biomedical applications, *Adv. Mater.* (30) (2018) 1801350.
- [20] W. Wu, D. Mao, F. Hu, S. Xu, C. Chen, C.-J. Zhang, X. Cheng, Y. Yuan, D. Ding, D. Kong, B. Liu, A highly efficient and photostable photosensitizer with near-infrared aggregation-induced emission for image-guided photodynamic anticancer therapy, *Adv. Mater.* (17) (2017) 1700548.
- [21] M. Ethirajan, Y. Chen, P. Joshi, R.K. Pandey, The role of porphyrin chemistry in tumor imaging and photodynamic therapy, *Chem. Soc. Rev.* (40) (2011) 340–362.
- [22] S. Singh, A. Aggarwal, N.V.S.D.K. Bhupathiraju, G. Arianna, K. Tiwari, C.M. Drain, Glycosylated porphyrins, phthalocyanines, and other porphyrinoids for diagnostics and therapeutics, *Chem. Rev.* (115) (2015) 10261–10306.
- [23] J. Zhao, K. Xu, W. Yang, Z. Wang, F. Zhong, The triplet excited state of BODIPY: formation, modulation and application, *Chem. Soc. Rev.* (44) (2015) 8904–8939.
- [24] T. Yogo, Y. Urano, Y. Ishitsuka, F. Maniwa, T. Nagano, Highly efficient and photostable photosensitizer based on BODIPY chromophore, *J. Am. Chem. Soc.* (127) (2005) 12162–12163.
- [25] B.M. Barth, E.I. Altinoğlu, S.S. Shanmugavelandy, J.M. Kaiser, D. Crespo-Gonzalez, N.A. DiVittore, C. McGovern, T.M. Goff, N.R. Keasey, J.H. Adair, T.P. Loughran, D.F. Claxton, M. Kester, Targeted indocyanine-green-loaded calcium phosphosilicate nanoparticles for in vivo photodynamic therapy of leukemia, *ACS Nano* (5) (2011) 5325–5337.
- [26] M. Guo, H. Mao, Y. Li, A. Zhu, H. He, H. Yang, Y. Wang, X. Tian, C. Ge, Q. Peng, X. Wang, X. Yang, X. Chen, G. Liu, H. Chen, Dual imaging-guided photothermal/photodynamic therapy using micelles, *Biomaterials* (35) (2014) 4656–4666.
- [27] S. Zhen, S. Wang, S. Li, W. Luo, M. Gao, L.G. Ng, C.C. Goh, A. Qin, Z. Zhao, B. Liu, B.Z. Tang, Efficient red/near-infrared fluorophores based on benzo [1,2-b:4,5-b'] di-thiophene 1,1,5,5-tetraoxide for targeted photodynamic therapy and in vivo two-photon fluorescence bioimaging, *Adv. Funct. Mater.* (28) (2018) 1706945.
- [28] L. Yao, S. Zhang, R. Wang, W. Li, F. Shen, B. Yang, Y. Ma, Highly efficient near-infrared organic light-emitting diode based on a butterfly-shaped donor-acceptor chromophore with strong solid-state fluorescence and a large proportion of radiative excitons, *Angew. Chem. Int. Ed.* (53) (2014) 2119–2123.
- [29] W. Li, Y. Pan, R. Xiao, Q. Peng, S. Zhang, D. Ma, F. Li, F. Shen, Y. Wang, B. Yang, Y. Ma, Employing ~100% excitons in OLEDs by utilizing a fluorescent molecule with hybridized local and charge-transfer excited state, *Adv. Funct. Mater.* (24) (2014) 1609–1614.
- [30] J. Li, K. Pu, Development of organic semiconducting materials for deep-tissue optical imaging, phototherapy and photoactivation, *Chem. Soc. Rev.* (48) (2019) 38–71.
- [31] G. Hong, A.L. Antaris, H. Dai, Near-infrared fluorophores for biomedical imaging, *Nat. Biomed. Eng.* (1) (2017) 0010.
- [32] A.L. Antaris, H. Chen, K. Cheng, Y. Sun, G. Hong, C. Qu, S. Diao, Z. Deng, X. Hu, B. Zhang, X. Zhang, O.K. Yaghi, Z.R. Alamparambil, X. Hong, Z. Cheng, H. Dai, A small-molecule dye for NIR-II imaging, *Nat. Mater.* (15) (2016) 235.
- [33] N.S. Makarov, M. Drobizhev, A. Rebane, Two-photon absorption standards in the 550–1600 nm excitation wavelength range, *Optic Express* (16) (2008) 4029–4047.
- [34] A.Z. Wang, R. Langer, O.C. Farokhzad, Nanoparticle delivery of cancer drugs, *Annu. Rev. Med.* (63) (2012) 185–198.
- [35] R. Tong, L. Tang, L. Ma, C. Tu, R. Baumgartner, J. Cheng, Smart chemistry in polymeric nanomedicine, *Chem. Soc. Rev.* (43) (2014) 6982–7012.
- [36] X. Yi, D. Zhao, Q. Zhang, J. Xu, G. Yuan, R. Zhuo, F. Li, A co-delivery system based on a reduction-sensitive polymeric prodrug capable of loading hydrophilic and hydrophobic drugs for combination chemotherapy, *Polym. Chem.* (7) (2016) 5966–5977.
- [37] X. Yi, J. Dai, Y. Han, M. Xu, X. Zhang, S. Zhen, Z. Zhao, X. Lou, F. Xia, A high therapeutic efficacy of polymeric prodrug nano-assembly for a combination of photodynamic therapy and chemotherapy, *Commun. Biol.* (1) (2018) 202.
- [38] W. Chen, F. Meng, F. Li, S.-J. Ji, Z. Zhong, pH-Responsive biodegradable micelles based on acid-labile polycarbonate hydrophobe: synthesis and triggered drug release, *Biomacromolecules* (10) (2009) 1727–1735.
- [39] R. Sun, Q. Luo, C. Gao, Y. Wang, L. Gao, H. Du, Y. Huang, X. Li, Z. Shen, W. Zhu, Facile fabrication of reduction-responsive nanocarriers for controlled drug release, *Polym. Chem.* (5) (2014) 4879–4883.
- [40] X. Duan, J. Xiao, Q. Yin, Z. Zhang, H. Yu, S. Mao, Y. Li, Smart pH-sensitive and temporal-controlled polymeric micelles for effective combination therapy of doxorubicin and disulfiram, *ACS Nano* (7) (2013) 5858–5869.
- [41] B. Tesfamariam, Bioresorbable vascular scaffolds: biodegradation, drug delivery and vascular remodeling, *Pharmacol. Res.* (107) (2016) 163–171.
- [42] N. Kamaly, B. Yameen, J. Wu, O.C. Farokhzad, Degradable controlled-release polymers and polymeric nanoparticles: mechanisms of controlling drug release, *Chem. Rev.* (116) (2016) 2602–2663.
- [43] Y. Wei, Z. Xue, Y. Ye, Y. Huang, L. Zhao, Paclitaxel targeting to lungs by way of liposomes prepared by the effervescent dispersion technique, *Arch. Pharm. Res.* (Seoul) (37) (2014) 728–737.